Monitoring local redox processes in LiNi$_{0.5}$Mn$_{1.5}$O$_4$ battery cathode material by in operando EPR spectroscopy

Arvid Niemöller, Peter Jakes, Svitlana Eurich, Anja Paulus, Hans Kungl, Rüdiger-A. Eichel, and Josef Granwehr

Monitoring local redox processes in LiNi$_{0.5}$Mn$_{1.5}$O$_4$ battery cathode material by *in operando* EPR spectroscopy

Arvid Niemöller,[1] Peter Jakes,[1] Svitlana Eurich,[1] Anja Paulus,[1] Hans Kungl,[1] Rüdiger-A. Eichel,[1,2] and Josef Granwehr[1,3]

[1]*Forschungszentrum Jülich GmbH, Institut für Energie- und Klimaforschung (IEK-9), 52425 Jülich, Germany*
[2]*Institut für Physikalische Chemie, RWTH Aachen University, 52056 Aachen, Germany*
[3]*Institut für Technische und Makromolekulare Chemie (ITMC), RWTH Aachen University, 52056 Aachen, Germany*

Despite the multitude of analytical methods available to characterize battery cathode materials, identifying the factors responsible for material aging is still challenging. We present the first investigation of transient redox processes in a spinel cathode during electrochemical cycling of a lithium ion battery by *in operando* electron paramagnetic resonance (EPR). The battery contains a LiNi$_{0.5}$Mn$_{1.5}$O$_4$ (LNMO) spinel cathode, which is a material whose magnetic interactions are well understood. The evolution of the EPR signal in combination with electrochemical measurements shows the impact of Mn^{3+} on the Li$^+$ motion inside the spinel. Moreover, state of charge dependent linewidth variations confirm the formation of a solid solution for slow cycling, which is taken over by mixed models of solid solution and two-phase formation for fast cycling due to kinetic restrictions and overpotentials. Long-term measurements for 480 h showed the stability of the investigated LNMO, but also small amounts of cathode degradation products became visible. The results point out how local, exchange mediated magnetic interactions in cathode materials are linked with battery performance and can be used for material characterization. *Published by AIP Publishing.* https://doi.org/10.1063/1.5008251

INTRODUCTION

High-voltage spinel cathode materials are promising candidates for next-generation lithium-ion batteries because they offer high operation voltages up to 5 V and thus enhanced energy density.[1,2] In that regard, the specific composition LiNi$_{0.5}$Mn$_{1.5}$O$_4$ (LNMO) is the most promising[3–6] and furthermore offers fabrication of cobalt-free batteries, considering that cobalt is a potentially scarce material when lithium-ion batteries are produced in higher quantities.

Prior to commercialization, however, mechanisms leading to materials degradation during cyclic operation have to be overcome. Corresponding insights can only be obtained when performing *in situ* or *in operando* type of experiments. In recent years, substantial efforts have been made in the area of *in operando* experiments to unravel the underlying mechanisms leading to materials degradation. Various methods have been employed to probe charge dependent properties of the spinel material. ^{7}Li nuclear magnetic resonance (NMR) measurements resolved the impact of reversible (de)lithiation to alter materials' structure.[7] EXAFS (extended X-ray absorption fine structure) measurements were used to monitor changes in bond lengths and coordination environments.[8] XANES (X-ray absorption near edge structure) investigations gave evidence for a distribution in oxidation states of manganese (III) and (IV) and nickel (II),(III), and (IV) at layers close to the particle surface.[9] Finally, by employing neutron powder diffraction, a shift of the LNMO reflection angle was reported that was correlated to a change of volume and lithium content.[10] Another recently developed technique for battery analysis is

in operando SQUID magnetometry, showing the overall material magnetism and changes thereof during battery cycling.[11,12] However, so far only *ex situ* measurements have been performed using SQUID magnetometry for LNMO samples, indicating that exchange interactions and magnetism present a very diverse probe for oxidation and structural changes in the material.[5,13,14]

Generally, LNMO spinel can be distinguished between a disordered, non-stoichiometric structure LiNi$_{0.5}$Mn$_{1.5}$O$_{4-\delta}$ ($Fd\bar{3}m$) and an ordered structure LiNi$_{0.5}$Mn$_{1.5}$O$_4$ ($P4_332$).[15–17] When the disordered LNMO is cycled vs. metallic lithium, a characteristic voltage profile is obtained. First, manganese oxidation of Mn^{3+} to Mn^{4+} takes place in the 4 V region. Subsequently, the high volt nickel oxidation occurs in two steps: first, Ni^{2+} to Ni^{3+} oxidation up to 4.7 V and afterwards Ni^{3+} to Ni^{4+} oxidation.[2,18–21] It has been proposed that for the cation-disordered spinel, Mn^{3+} species, which are associated with oxygen defects, affect the LNMO defect structure[16,22] and enhance Li$^+$ transport.[23] Furthermore, Mn^{3+} causes a Jahn-Teller distortion, affecting the exchange interactions with nickel.[8,9,19,24]

Because nickel and manganese are, depending on their oxidation state, electron paramagnetic resonance (EPR) active,[25] relevant atomic-scale information can be gathered. Since the effect of cyclic aging shall be studied, the *in operando* mode of operation is mandatory to exclude damages during post-test preparation of specimens. The corresponding EPR spectra are, however, expected to consist of multiple overlapping components, as both ions are octahedrally coordinated. Moreover, an electron interaction of both species takes place,

enabling, e.g., exchange and super-exchange couplings.[13,14,26] This can lead to exchange narrowing in EPR, which is an effect of exchange coupled paramagnetic centers that narrows the EPR linewidth inversely proportional to the exchange constant.[27] Therefore, in a material where exchange interactions are changing during the course of an experiment, e.g., due to redox processes of the involved ions or due to alterations in the lattice, the EPR linewidth represents a very sensitive probe for such variations. In the following, the lengthscale over which exchange is active is referred to as *local*.

By performing *in operando* EPR experiments, fundamental electrochemical redox reactions can be monitored while physical and chemical properties are changing. Distortions of results due to sample handling, which occur during *in situ* or *ex situ* measurements, are minimized.[28] Furthermore, the combination of at least two simultaneously recorded analytical methods, e.g., spectroscopic and electrochemical data, drastically augments a meaningful data interpretation.[29,30] Up to now, EPR spectroscopy has rarely been used for *in operando* battery measurements. The formation of different lithium morphologies[31] and of singlet oxygen in lithium air batteries[32] was observed. In addition, by *in situ* EPR imaging, the formation and transformation of metallic lithium was monitored during battery cycling.[33] However, previous *in operando* EPR cell designs did not allow for long-term operation with cycle numbers that are relevant for the typical lifetime of a battery cell. Since cathode materials such as LNMO only show broad EPR signals with weak intensity, an optimized cell design is necessary to detect cathode material changes during cycling with good sensitivity to facilitate a sufficiently high temporal resolution. The LNMO spinel is particularly suitable for such a study due to its good cycling stability,[1–6] facilitating the undisturbed identification of redox processes as a function of cycling rates without dominant contributions from degradation. Moreover, the material is well understood in terms of magnetic interactions to support the EPR data evaluation.

Taking into account the different requirements for electrochemical and spectroscopic investigations, we present a novel flat cell battery design suitable for long-run *in operando* EPR

measurements. Based on this design, a battery with LNMO spinel produced by solid-state synthesis as cathode material has been constructed and investigated *in operando* simultaneously by EPR and electrochemically. Charging and discharging at different rates as well as cyclic voltammograms (CVs) were recorded on a single cell over the course of several hundred hours, acquiring EPR spectra simultaneously. The EPR signal amplitude was calculated as an indicator for the changing susceptibility of the material and correlated with electrochemical data. Thereby, information was obtained about oxidation states, rate capacity, and EPR activity of LNMO cathode material. Thermodynamic as well as kinetic processes could be correlated, and influences of external potentials were identified.

RESULTS

Electrochemistry

The chemically active materials were stacked into a newly developed quartz glass support as shown in Fig. 1. On the anode side, metallic lithium was positioned on top of the copper current collector. On the cathode side, LNMO was coated on Celgard and placed on top of the aluminum current collector. A synthetic ruby was positioned in a hole above the cell as EPR reference and a PFA (polyfluroalkoxy) stick for spacing adjustments in another hole below (for detailed construction and theoretical considerations, see Note 1 and Method 1 of the supplementary material).

This flat cell setup shows a stable performance over 45 cycles, with a total experiment duration of 480 h, during operation in the EPR resonator. Figure 2 shows the cell performance at different cycling rates ranging from C/20 to 5C. The initial and the final C/20 cycle [Fig. 2(a)] both show Mn^{3+}/Mn^{4+} oxidation in the 4 V region and subsequently Ni^{2+}/Ni^{3+} and Ni^{3+}/Ni^{4+} oxidation, indicated by two plateaus, at about 4.6 V and 4.7 V, respectively, which is typical for LNMO.[2,18] A small capacity reduction of about 5% is found for the final compared to the initial cycle. The C/5 cycles [Fig. 2(b)] still
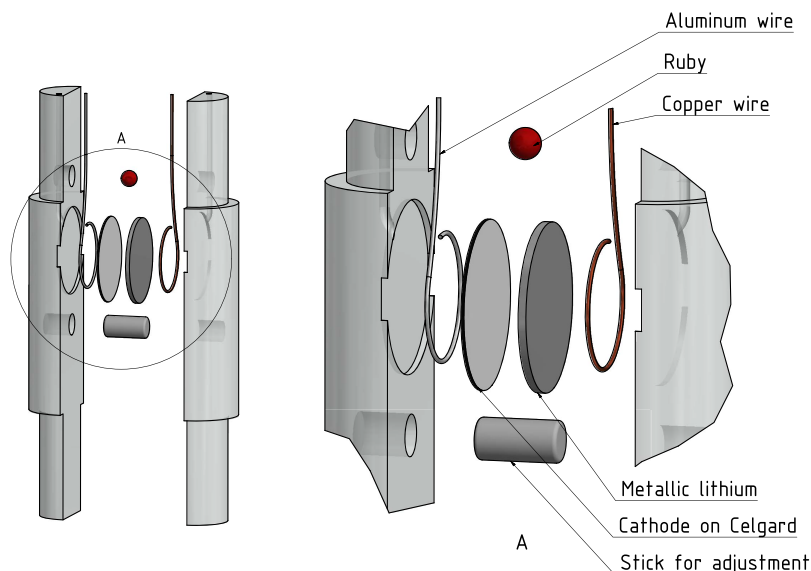

FIG. 1. Schematic of the *in operando* EPR battery cell. The quartz glass casing is shown with an exploded view of the battery materials' stacking. The cell has a height of 40 mm and a diameter of 8 mm.

Aluminum wire
Ruby
Copper wire
Metallic lithium
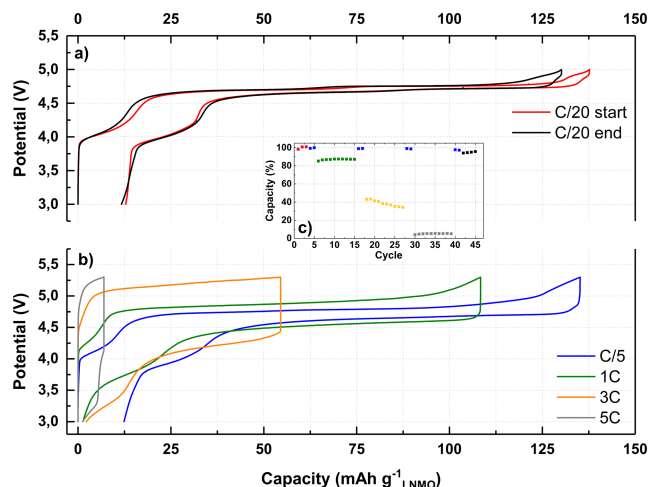Cathode on Celgard
Stick for adjustment

FIG. 2. *In operando* battery cycling performance. (a) C/20 cycles at the start and end of experiments show slightly different capacities. One manganese and two nickel transitions are resolved. (b) C/5, 1C, 3C, and 5C rates show a strong increase in overpotentials as rates increase. (c) Discharge capacity relative to the first slow cycles at C/20 for cycling rates shown in (a) and (b).

show nearly the same capacity as the C/20 rates, but the overpotential starts to become apparent, leading already to a reduced voltage efficiency. A decrease in charge and discharge capacity due to overpotentials and polarization effects is detected at a 1C rate, yet both nickel plateaus are still contributing to the cell capacity, although the transition between the two plateaus is not clearly resolved any more. 3C and 5C cycles are dominated by overpotentials. Although the upper voltage limit was set substantially above the Ni^{3+}/Ni^{4+} potential at 5.3 V, the single wire loops used as current collector as well as bottlenecks in the Li ion transport limit the electron transfer at high current densities. These overpotentials shift the nickel transitions to even higher voltages, which were out of the experimental range given by the stability of the electrolyte.

Along with increasing overpotential at high rates the capacity of the cell dropped close to zero for 5C cycles [Fig. 2(c)]. Charging rates faster than C/5 result in a decrease in the Faraday efficiency to 76% at 1C and to ca. 5% at 5C cycles. Thus, for *in operando* measurements, slow cycles are most suitable due to the high voltage resolution and low overpotentials.

At a charging rate of C/20, the plateau for the Mn^{3+}/Mn^{4+} oxidation starts to considerably increase about half way before the Ni^{2+}/Ni^{3+} plateau is reached, while the Mn^{4+}/Mn^{3+} reduction plateau shows a steeper edge at the end of the Ni^{3+}/Ni^{2+} plateau. At C/5 and 1C, the Mn^{3+}/Mn^{4+} oxidation plateau gets even shorter before it starts to increase, while the reduction plateau retains its width, but the edge to the Ni^{3+}/Ni^{2+} plateau gets broader. At 3C, the oxidation plateau is hardly visible, while the reduction plateau gets shorter.

While cycling at increased rates led to a considerable capacity reduction, it did not lead to a drastic long-term battery degradation, as reverting to slow cycling also recovered the initial capacity at that rate.

Electron paramagnetic resonance

The pristine battery resulted in multiple EPR resonances, as shown in Fig. 3(a). The broad LNMO signal ranged from ca.

150 mT to 500 mT, exhibiting a lineshape that is Lorentzian in its center but falls off more rapidly at the wings, which is typical for exchange narrowed, strongly coupled paramagnetic centers.[27] A narrow Dysonian signal from metallic lithium was found at 330 mT. The Lorentzian peaks at 189 mT, 317 mT, and 531 mT originated from the ruby reference. Due to their minimal overlap with other resonances, the two outer peaks can be fitted well with a Lorentzian line and therefore were used for phase and amplitude correction.

The LNMO EPR signal shows a characteristic development during battery cycling (Fig. 4). The intensity and the linewidth of the cathode material changed synchronously during charge and discharge for low C rates. Using the battery potential, these changes could be correlated with oxidation or reduction processes occurring in the LNMO material. For a simplified discussion, the evolution of the EPR signal intensity and battery potential at C/20 rate is grouped into different processes which are labeled with Roman numbers in Fig. 4. First, an increase in and a simultaneous narrowing of the LNMO EPR signal during process (I) took place, which could be correlated with the Mn^{3+}/Mn^{4+} transition according to the electrochemical curve. From the width of process (I) relative to the combined width of processes (II) and (III), a ratio of $[Mn^{3+}]/[Ni_{tot}]$ ≈ 0.27 in the discharged battery can be estimated leading to a $LiNi_{0.5}Mn_{1.5}O_{4-\delta}$ stoichiometry with $\delta \approx 0.068$. While in the stoichiometric compound $LiNi_{0.5}Mn_{1.5}O_4$ no Mn^{3+} would be expected, it is well documented that LNMO can show a Ni deficit ($LiNi_{0.5-x}Mn_{1.5+x}O_4$) or oxygen vacancies ($LiNi_{0.5}Mn_{1.5}O_{4-\delta}$) that lead to the presence of Mn^{3+}.[16]

Subsequently, during process (II) Ni^{2+} was partially oxidized to Ni^{3+}, which led to a decrease in and a simultaneous broadening of the LNMO EPR signal. The slopes $m_{(I)}$ and $m_{(II)}$ of the signal intensity change during process (I) and (II), respectively, have approximately identical amplitude and opposite sign, with $|m_{(I)}| \approx 3.3$ and $|m_{(II)}| \approx 3.0$ (in arbitrary units). The signal change accelerates during process (III) to $|m_{(III)}| = 5.5$. Moreover, the LNMO EPR resonances during processes (I) and (II) are found to have a synchronous development of the linewidth, which indicates a correlation between the lattice positions of Mn^{3+} ions oxidized during process (I) and the Ni^{2+} ions oxidized during (II). A slight increase in the nickel plateau at 4.7 V indicated the complete oxidation of Ni^{2+} at the end of process (III), which was accompanied by a clearly visible kink in the EPR signal slope and a plateauing, followed by a subsequent minor drop of the linewidth when process (IV) was reached. As suggested in the literature,[21] during process (IV) oxidation of Ni^{3+} to Ni^{4+} took place. Notice that there is no indication in the signal amplitude of a similar segregation of the Ni^{3+}/Ni^{4+} transition into two processes as was the case for the Ni^{2+}/Ni^{3+} oxidation. Complete nickel oxidation was achieved and the discharging was stopped when the potential reached 5 V. A broad EPR signal with an amplitude of about 25% of the maximum signal remained.

Process (V) marks the battery discharging process that shows the same trends as the charging process (I) to (IV) in reverse order. Both the amplitude and width of the EPR lines were almost completely reversible at C/20, only dependent on the state of charge (SOC) of the battery.
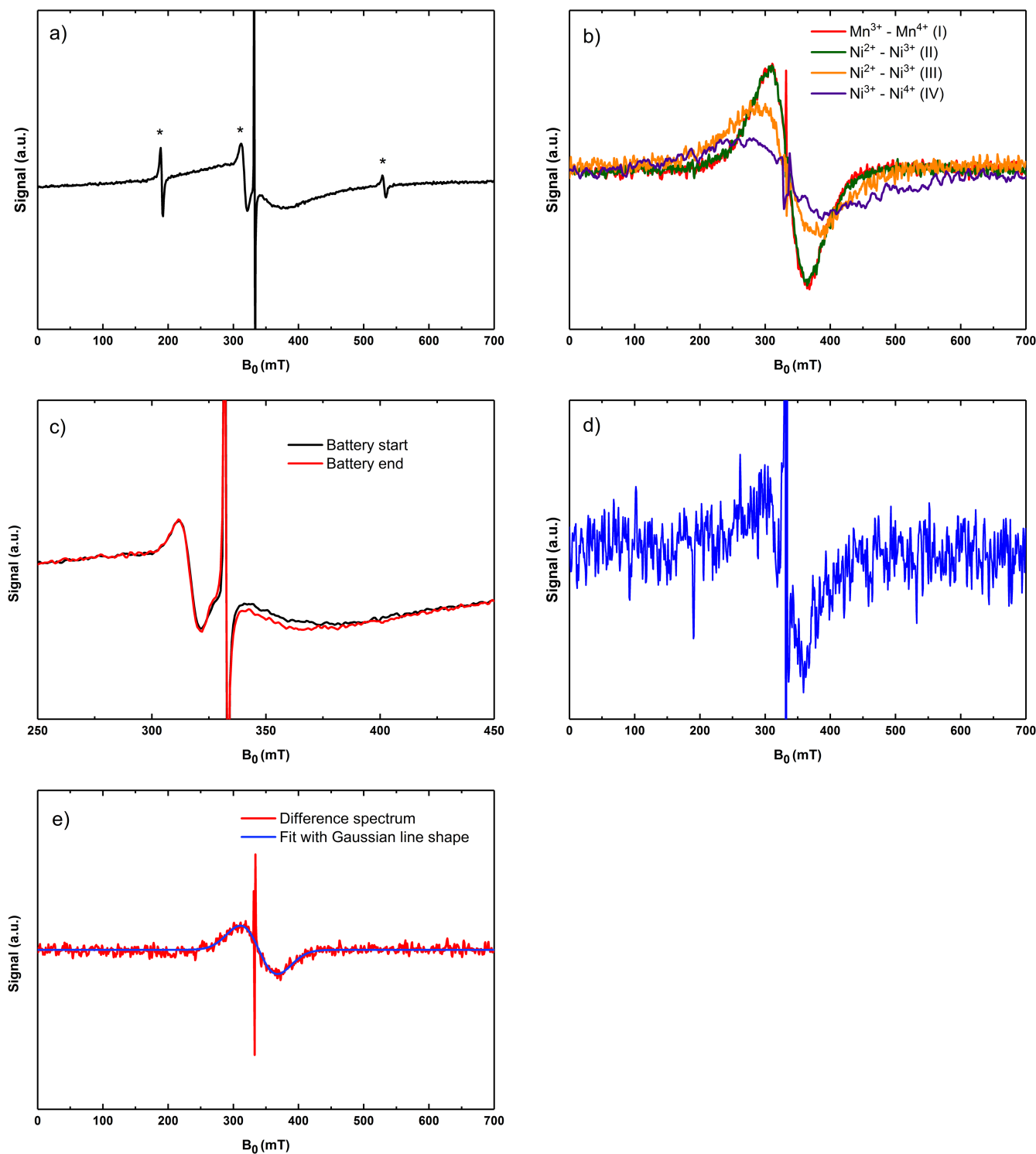
FIG. 3. EPR first derivative spectra recorded *in operando*. (a) EPR spectrum of the pristine *in operando* cell. Lithium signal at 330 mT, broad LNMO signal from 150 mT to 500 mT, and ruby reference signals at 189 mT, 317 mT, and 531 mT marked with a star (∗) can be distinguished. (b) Difference spectra for the main four redox processes (I)-(IV) during battery charging. Processes (I) and (II) show the same linewidth and intensity. Further charging leads to a broadening during process (III). (c) Cathode material changes over 500 h. Comparison of the EPR spectrum of the pristine battery and the cycled battery after the final C/20 cycle in the discharged state. (d) The difference spectrum between the pristine and the aged battery shows a narrow component with $\Delta B \approx 45$ mT. (e) Difference spectrum for the Ni^{2+}/Ni^{3+} transition between charge and discharge processes for a C/5 cycle. The EPR signal is fitted with a Gaussian lineshape that hints at a distribution of linewidths for the sites responsible for this spectrum.

While the linewidth was changing considerably as a function of the SOC, fitting the LNMO signal with a single Lorentzian was possible with a consistent quality during a charge/discharge cycle of the battery. This indicates that the LNMO resonance was changing more or less continuously during cycling rather than observing a superposition of multiple components in the spectrum that are weighted according to the SOC of the battery. This is particularly significant during
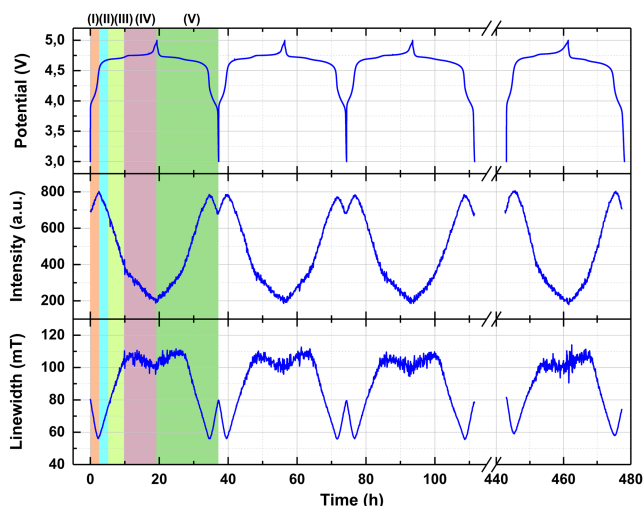
FIG. 4. Comparison of electrochemical and spectroscopic data. Electrochemical curve of battery cycling with C/20 (top), intensity of the LNMO EPR signal from a fit of the first derivative of a Lorentzian line to the experimental spectrum (central panel), and signal linewidth of the LNMO EPR signal (bottom). (I) oxidation of Mn^{3+} to Mn^{4+}, (II) partial oxidation of Ni^{2+} to Ni^{3+}, (III) complete oxidation of Ni^{2+} to Ni^{3+}, and (IV) oxidation of Ni^{3+} to Ni^{4+}. Process (V) marks the discharging process including the steps (I)–(IV) in reverse order.

processes (I) to (III), where the linewidth change is considerable. During process (IV), the quite small change does not allow for a conclusive distinction between a continuous change and a superposition of two lines with similar width.

Fast cycling rates significantly changed the character of the LNMO EPR lines. While the amplitude was affected only moderately, the linewidth changed significantly less as a function of SOC for 1C and 3C than for C/20 (Fig. 5), and the linewidth became asymmetric when comparing charge and discharge at identical SOC during processes (III) and (IV) with the corresponding periods during process (V). Figure 3(e) shows a difference spectrum for a C/5 charge and discharge cycle
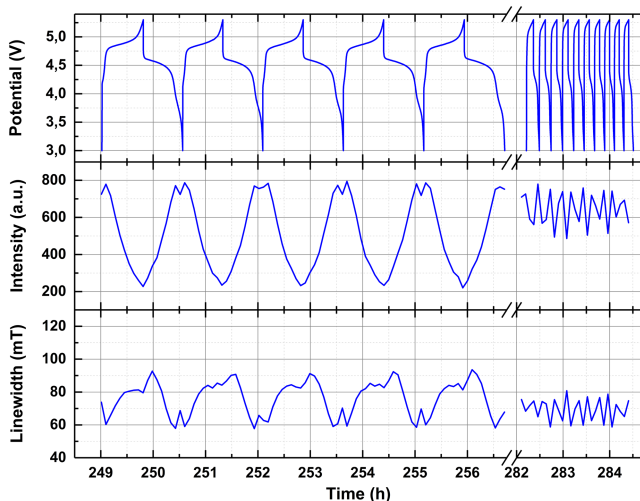

FIG. 5. Comparison of electrochemical and spectroscopic data for fast cycling rates. Electrochemical curve of battery cycling with 1C (left) and 3C (right) at the top, signal intensity of the LNMO EPR signal (central panel), and signal linewidth of the LNMO EPR signal (bottom). Intensity and linewidth change drastically with increasing cycling rate from 1C to 3C.

at the transition point between process (II) and (III). In contrast to the broad LNMO line, where Lorentzian lineshapes provided good fits, a Gaussian lineshape showed the best fit in this case, pointing towards a distribution of EPR active species responsible for this line.

1C rates still indicated nickel and manganese transitions as demonstrated in Fig. 5. However, process (IV) was shortened compared to C/20, which is consistent with an incomplete oxidation as also suggested by the electrochemical data in Fig. 2(b). For 3C rates, the current resolution of the EPR measurements is insufficient for a meaningful tracking of the redox processes. Nonetheless, the EPR signal changed synchronously with the current deposited or extracted. The intensity remained high and the linewidth remained low throughout, consistent with only a partial Li extraction at high C rates.

Figure 3(b) shows the difference spectra for the processes discussed previously. The spectra at the start and end of each process were subtracted, obtaining the signal change. Difference spectra for processes (I) and (II) show the same linewidth and intensity, which indicates changes of the same EPR active species. The linewidth increases for the difference signal of complete Ni^{2+} oxidation (III) and further for Ni^{3+} oxidation (IV).

The EPR spectra of the discharged battery at the beginning and at the end of the battery test are compared in Fig. 3(c). Small deviations of the LNMO peak were obtained that show the existence of an additional narrow signal component at the end of battery operation. While the initial linewidth of LNMO is $\Delta B \approx 80$ mT, this second component only has a linewidth of $\Delta B \approx 45$ mT [Fig. 3(d)]. This additional signal was found at all potentials in the last C/20 cycle, hence it appears to originate from a sample region that became electrochemically inactive during cycling.

Mn^{2+} dissolved in the electrolyte could, in principle, be resolved as well. In the current experiments, which were acquired with parameters optimized for the broad LNMO signal, such Mn^{2+} species are only scantly visible in accumulated spectra. The signal intensity is consistent with a sub-ppm Mn^{2+} concentration in the electrolyte, which was also found in a $Li_{1.2}Ni_{0.15}Mn_{0.55}Co_{0.1}O_2$-based Li-ion cell.[34] For a more quantitative assessment, additional experiments with different parameters would be necessary.

During the entire cycling procedure, changes of the metallic lithium signal amplitude were detected that were anti-cyclical in comparison to the LNMO signal. Battery charging, when Li was extracted from the LNMO cathode and deposited in the form of "mossy lithium" on the metallic Li anode, led to an increase in the metallic lithium signal amplitude, discharging caused a decreasing amplitude.[31] However, the acquisition parameters were not suitable for a detailed interpretation of the conduction EPR signal of Li metal, hence this resonance is not considered further.

DISCUSSION

Interpretation of EPR spectra

EPR spectroscopy selectively detects spin magnetic moments. For 3d transition metal ions, the spin-only approach

can be used to calculate the EPR susceptibility by using $\chi \propto S(S+1)$, where S is the spin quantum number of a particular ion. Table I shows the different oxidation states of manganese and nickel with the corresponding spins for an octahedral coordination of the ion. The spin-only scaling for each species and the susceptibility changes upon oxidation were calculated. However, susceptibility changes as shown by the signal amplitude in Fig. 4 (central panel) do not correlate with the values obtained by the spin-only approach.
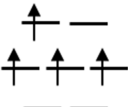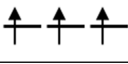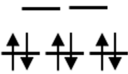
This is probably, at least to some degree, caused by considerable oxidation state dependent variations of exchange couplings between the transition metals or super-exchange couplings via oxygen. Without exchange narrowing, the EPR spectra of high-spin Mn and Ni ions are challenging to detect at X-band frequencies due to strongly anisotropic interactions and often large zero-field splitting.[25] Furthermore, lines are additionally broadened in materials with stoichiometric concentrations of these paramagnetic centers due to fast relaxation. Other than for dilute centers in a diamagnetic matrix, a quantitative analysis of EPR data becomes very demanding for these ions and generally requires individual calibration experiments.[13,26,35]

Mn^{3+} typically has extremely broad or not visible signals in X-band EPR spectroscopy. Therefore, despite susceptibility reduction, signal increase upon oxidation from Mn^{3+} to Mn^{4+} can be referred to the increase in Mn^{4+} content in process (I) in Fig. 4. Processes (I) and (II) show similar but opposite slopes and equal linewidths in the difference spectra in Fig. 3(b). This symmetry indicates some exchange interaction developing during Mn^{3+} to Mn^{4+} oxidation with those Ni^{2+} ions that are oxidizing during process (II). Therefore, the two ions are located in spatially close lattice positions. Furthermore, it hints that these Ni^{2+} ions in spatial vicinity to Mn^{3+} in the discharged material are the first ones to be oxidized to Ni^{3+} once all Mn^{3+} are oxidized. Electrochemically, this could be explained by

a slightly lower redox potential for these nickel ions as seen in Fig. 4, where the plateau for the Ni^{2+} to Ni^{3+} oxidation is only reached at the end of process (II). While this may have a minor negative impact on the theoretical battery energy, a much more significant effect is that one Ni/Mn^{3+} is only oxidized to Ni^{3+} since one Li^+ is extracted at the Mn^{3+}/Mn^{4+} potential. Consequently, the presence of Mn^{3+} reduces the amount of Li^+ that is extracted at the high Ni potential. In particular, despite the exquisite sensitivity of the EPR resonance to variations in the immediate, local environment of an ion, the change in signal slope and linewidth upon Ni^{2+}/Ni^{3+} oxidation between processes (II) and (III) has no correspondence in process (IV), suggesting that the Ni^{2+} ions in the vicinity of Mn^{3+} in the stoichiometric material only get oxidized to Ni^{3+}. This is intuitively plausible since these are the Ni ions whose environment has already been depleted of one Li^+. Using this argument in reverse, it demonstrates that the occurrence of exchange interactions and the corresponding EPR linewidth change is correlated with and potentially has a similar origin as variations of the electrochemical potential of a particular ion. The spatial vicinity of Mn^{3+} and Ni^{2+} contradicts reasoning based on charge neutrality arguments presented in Ref. 13 that suggested a preferred Mn^{4+} surrounding for Mn^{3+} ions, yet it is not incompatible with data presented therein. Process (IV) exhibits Ni^{3+} to Ni^{4+} oxidation with a slower change of signal intensity than process (III). The change of susceptibility is expected to be slower as shown in Table I which becomes apparent with the ratio of slopes $m_{(III)}/m_{(IV)} \approx 2.5$.

The variation of the LNMO signal linewidth (Fig. 4) is in accordance with SQUID measurements on *ex situ* samples at cryogenic temperatures by Moorhead-Rosenberg *et al.*[13] who found an increasing magnetic moment and therefore stronger exchange coupling with decreasing Mn^{3+} content. At room temperature, no magnetic ordering is expected, yet such an increased exchange coupling leads to a more

TABLE I. Electron spin configuration of manganese and nickel. In LNMO octahedral, complexes of both transition metals are found. The spin-only approach for 3d transition metals is an approximation and does not include any exchange interactions. During cycling the spin configuration changes and susceptibility of the spin-only approach scales with $\Delta(S(S+1))$.

Transition metal ion	Spin	Octahedral spin complex	$\chi \propto S(S+1)$	$\Delta(S(S+1))$
Mn^{3+}	4/2	High spin complex	6	
				2.25
Mn^{4+}	3/2		3.75	
Ni^{2+}	2/2		2	
				1.25
Ni^{3+}	1/2	Low spin complex	0.75	
				0.75
Ni^{4+}	0		0	

effective exchange narrowing of the EPR resonances and narrower lines as the potential increases during process (I). As Ni^{2+} oxidation takes place during processes (II) and (III), EPR intensity decreases. Since Ni^{3+} is not involved in exchange interactions,[36] exchange narrowing gets reduced, leading to broader EPR lines. During process (IV), exchange interactions are not changing appreciably, leading to a more or less constant linewidth that gets only slightly narrowed.

Complete nickel oxidation results in an EPR silent Ni^{4+} state with $S = 0$. Still, about 25% of the signal amplitude remains in the form of a very broad signal with a linewidth of $\Delta B \approx 100$ mT. From the previously estimated ratio of $[Mn^{3+}]/[Ni_{tot}] \approx 0.27$ in the pristine material, approximately one quarter of Ni should still be in the paramagnetic Ni^{3+} state at the end of process (IV). In addition, Mn^{4+} can contribute to an EPR signal according to Table I. Exchange coupling of Mn^{4+} has not been reported with Ni^{3+} and is impossible with low-spin Ni^{4+}, implying that exchange narrowing is weaker for the fully charged battery. Nonetheless, at low temperatures Mn^{4+}–Mn^{4+} couple antiferromagnetically and Mn^{4+}–O–Mn^{4+} couple ferromagnetically.[26] These exchange interactions could be a reason that a manganese signal may still be contributing to the EPR signal at 5 V.

The LNMO EPR signals were fitted with a single Lorentzian component throughout. The quality of the fit did not significantly change during a charge/discharge cycle, which indicates that the redox processes inside the grains are homogenously distributed and a core–shell structure is unlikely. Furthermore, the considerable continuous variation of the EPR linewidth with consistent fit quality for the Mn^{3+}/Mn^{4+} as well as for the Ni^{2+}/Ni^{3+} oxidation [processes (I) to (III)] in particular for the C/20 cycles supports the formation of a solid solution rather than a two-phase formation. In the case of two-phase formation with one broad and one narrow line, it would be expected that upon cycling the relative intensities of the lines change, which would be accompanied by degrading residuals when fitting with a single Lorentzian line. During the Ni^{3+}/Ni^{4+} oxidation, the linewidth changes only weakly, which does not allow a conclusive distinction between solid solution and two-phase formation. This is in accordance with observations made by Wang *et al.*[17] that suggest the initial formation of a solid solution phase at a low degree of delithiation, followed by two-phase formation at higher degree of delithiation.

Long-term material degradation

The long-term stability of the material is demonstrated by the good capacity retention after 45 cycles (480 h of battery operation) and a nearly constant EPR intensity. In addition, at full charge of the fresh battery for C/20, only a single broad LNMO EPR signal could be distinguished, which indicates that all LNMO particles are contacted and cycled. In the aged battery, an electrochemically inactive contribution with a small amplitude and a narrow linewidth that was not changing during cycling became visible in the EPR spectrum [Fig. 3(d)]. The linewidth, which is even smaller than at the boundary between processes (I) and (II), indicates that the corresponding region is strongly affected by exchange narrowing and

therefore shows a high degree of magnetic as well as structural ordering. When compared to the other spectra, such a strong exchange narrowing is only expected in a region that contains Mn and Ni ions solely as Mn^{4+} or Ni^{2+}, respectively. However, from these data, it is not possible to distinguish whether this high degree of ordering is caused by a local structural change of the spinel, e.g., a transition from the disordered $Fd\bar{3}m$ into the ordered $P4_332$ phase,[37] or if sample regions which showed a high degree of structural ordering from the beginning got detached from the active part of the material. Nonetheless, this demonstrates a possible connection between high structural and magnetic ordering on the one hand and the loss of electrochemical activity during material degradation on the other hand.

Another indication for an onset of material degradation is the rounder edges of the EPR intensity at the transitions between different processes, best visible between processes (II) and (III) as well as between (III) and (IV) in Fig. 4. This is consistent with the less pronounced transition between different oxidation plateaus when comparing the C/20 voltage curves at the beginning and at the end of cycling in Fig. 2(a).

Cycling at increased rate

Fast cycling at a 1C rate shows similar trends for the EPR signal amplitude (Fig. 5) as at C/20. However, linewidth changes are considerably less pronounced, and particularly during processes (III) and (IV) significantly narrower lines are observed. This indicates that exchange narrowing due to Ni^{2+} is more pronounced during (III) and still takes place during (IV). Furthermore, the evolution of the linewidth is not symmetric between charge and discharge anymore. While the linewidth changes linearly during each process from (I) to (III) for C/20 cycles, which indicates a solid solution formation during manganese and Ni^{2+}/Ni^{3+} oxidation, 1C cycles exhibit significantly less linear and also smaller slopes for the linewidth changes during nickel oxidation and reduction. Mn^{3+}/Mn^{4+} oxidation and also Ni^{2+}/Ni^{3+} oxidation during process (II) still appear to be accompanied by the formation of a solid solution, but at the transition between processes (II) and (III) the behavior of the EPR signal changes qualitatively. A possible explanation could be a shifting balance between thermodynamic and kinetic control of the lithium extraction/insertion towards the latter during processes (III) and (IV). Rather than a uniform oxidation of Ni^{2+} to Ni^{3+}, regions within the sample accessible with lower overpotential may be fully oxidized before poorly connected regions start to get oxidized.

The fairly rapid increase in the linewidth once the battery was switched from charge to discharge highlights the transient nature of these effects, which rapidly relax into a thermodynamically more stable state once the external potential is altered. This shows that the balance between thermodynamic and kinetic processes is not only influenced by the C rate but also by the external potential, highlighting the importance of *in operando* experimental techniques for its observation and potential quantification.

When combined with electrochemical data in Fig. 2, these observations imply a model for Li ion dynamics in the LNMO
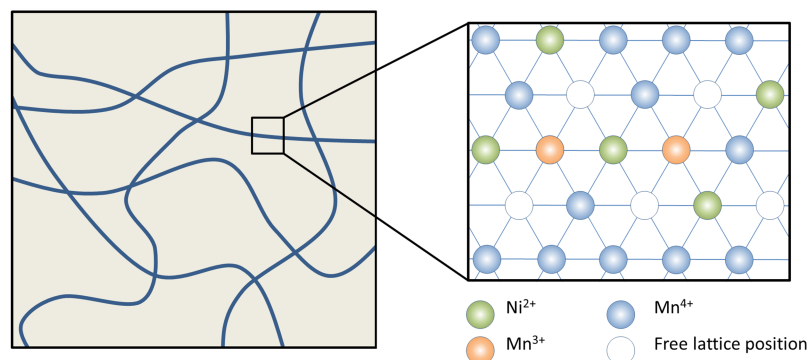
FIG. 6. Conceptual representation of lithium diffusion paths in Mn^{3+} rich areas. Lithium diffusion is enhanced in the spatial vicinity of oxygen vacancies,[18,23] hence the regions with high Mn^{3+} content show a faster lithium diffusion, also in terms of rate capability, in comparison to Mn^{3+} poor areas.

material and the role of Mn^{3+}. From Fig. 2, it is apparent that considerable overpotentials occur even at a moderate charge/discharge rate of C/5 and that charging to full capacity is not possible anymore at 1C. On the other hand, the Mn^{3+}/Mn^{4+} oxidation and reduction are less influenced by increased rates. EPR shows that the signal amplitude during Mn^{3+}/Mn^{4+} as well as during process (II) Ni^{2+}/Ni^{3+} oxidation and reduction is only little influenced up to a 1C rate. Therefore, Li ion motion is considerably faster in the vicinity of Mn^{3+}. The presence of Mn^{3+} was reported to be linked to oxygen vacancies, with an energetically preferred configuration of two Mn and one Ni as the nearest neighbor transition metals of an oxygen vacancy.[23]

The combined effect of the reduced charge of Mn^{3+} compared to Mn^{4+} and the presence of vacancies increases the local mobility of Li ions, which is not only limited to the extraction/insertion of a single Li^+ ion but a second Li^+ ion can benefit from this enhanced mobility as well, with charge compensation by a neighbouring Ni^{2+}/Ni^{3+} couple. However, this effect appears to be limited in range since segregation into processes (II) and (III) is fairly strict. It probably requires some structural adaptation for the Li outside the influence of Mn^{3+} centers to move, causing an activation barrier that leads to an activation overpotential. The C/20 voltage profiles [Fig. 2(a)] show that the Mn^{3+}/Mn^{4+} plateau is somewhat sloped but not strongly dependent on the C rate, indicating that a non-uniform overpotential exists, possibly for the transport of Li ions farther inside of the material. This suggests that Mn^{3+} sites are not only responsible for local mobility but they form the backbone of diffusion paths with enhanced long-range mobility that allows Li ions to move inside the material. Exchange of Li between these mobile paths and the regular lattice regions without Mn^{3+} and vacancies is slow, implying overpotentials at high C rates for the affected Ni^{2+}/Ni^{3+} and Ni^{3+}/Ni^{4+} oxidation couples. This model is sketched in Fig. 6, where microscopic vacancy-free domains are crossed by a network of lithium diffusion paths.

When cycling at an even higher rate of 3C, the electrochemical data show that the high voltage capacity is not reached anymore due to overpotentials. The EPR spectra only show variations of intensity and linewidth that barely go beyond processes (I) and (II). Based on the previously discussed results, it is likely that Ni^{2+} ions without Mn^{3+} centers or oxygen vacancies in their surrounding are preferably keeping their oxidation state since mass transport is kinetically limited during fast cycling. Only Li^+ ions close to Mn^{3+}

are mobile enough to support insertion/extraction into/out of the spinel structure and are therefore still cycled at a high rate.

CONCLUSION

Electrochemical and *in operando* EPR results have demonstrated the importance of Mn^{3+} in the LNMO spinel for the lithium transport and nickel redox behavior. Mn^{3+} looks to be located close to Ni^{2+} ions and causes an oxidation of these nickel species first once Mn^{3+} is completely oxidized during charge of a Li-ion battery. Although an increasing number of Mn^{3+} ions decrease the capacity, specifically the high voltage capacity, it beneficially lowers the charging overpotential. Therefore, the fast charging performance is improved, which is highly important, e.g., for electromobility. Mn^{3+} ions and the associated vacancies also play a crucial role for local as well as for long-range Li ion mobility within the LNMO material. Specifically, the flatness of the Ni^{2+}/Ni^{3+} and Ni^{3+}/Ni^{4+} potentials indicates that Li motion within vacancy-free (Mn^{4+}) regions of the material is not limited, but transition from Mn^{4+} regions into Mn^{3+} regions, where the long-range motion takes place, is more limiting.

The long-term *in operando* measurement allowed the identification of small material changes after more than 480 h of operation. A narrow additional EPR signal indicates the existence of electrochemically inactive regions with a high degree of local structural and magnetic ordering. If these regions were created by structural changes or if they were highly ordered from the beginning and lost their ionic or electric contact during battery operation, they cannot be distinguished without further experiments. In addition, a refined analysis will be performed by incorporation of a more detailed model for the lineshape in the presence of exchange narrowing. This will enable a more accurate distinction between different contributions to the signal and a quantitative identification of EPR inactive components during battery cycling.

SUPPLEMENTARY MATERIAL

See supplementary material for a detailed illustration of *in operando* hardware development, configuration, and cell performance.

APPENDIX: EXPERIMENTAL

Battery preparation

Metallic lithium was purchased from Sigma-Aldrich with 0.38 mm thickness and an assigned purity of 99.9%. The LNMO cathode material with a $Fd\bar{3}m$ crystal structure (shown in method 2 of the supplementary material) was synthesized by a solid state route. It was mixed with 10 wt. % carbon black (Alfa Aesar) and 10 wt. % polyvinylidene fluoride (PVDF) (Alfa Aesar) and coated on a 25 μm thick Celgard 3401 separator. The coated layer was not pressed and was 110 μm thick. 30 μl of 1M LiPF$_6$ in 1:1 w/w ethylene carbonate:dimethyl carbonate (LP30, BASF) was utilized as electrolyte. Connection wires were made from aluminium (Goodfellow, 0.25 mm diameter, 99.999% purity) and copper (Goodfellow, 0.25 mm diameter, 99.99+% purity).

Battery connectors as well as rings, spacers, and holders from PFA were made in-house. The quartz glass cell casing was fabricated by laser induced edging (LightFab GmbH, Aachen, Germany).

A spherical synthetic ruby (Goodfellow) with a diameter of 1.5 mm was used as EPR reference. Its signal was used for the data analysis to correct for phase, frequency, and amplitude changes due to a varying impedance of the battery during electrochemical cycling.

Electrochemical testing

Battery cycling was done with a Biologic SP-200 potentiostat. Charging and discharging as well as cyclic voltammogram (CV) curves were performed at different rates. The following galvanostatic cycling procedure was applied: (i) three C/20 cycles; (ii) two CVs with dE/dt = 0.028 mV; (iii) two C/5 cycles; (iv) ten C/1 cycles; (v) two C/5 cycles; (vi) ten 3C cycles; (vi) two C/5 cycles; (vii) ten 5C cycles; (viii) two C/5 cycles; and (ix) four C/20 cycles. Cycles with C/20 were performed between 3.0 and 5.0 V, and faster cycling between 3.0 and 5.3 V.

EPR spectroscopy

EPR measurements were performed on a Bruker ElexSys E540 X-band spectrometer in a 4108 TMHS resonator. The field sweep was set from 0 to 700 mT with a sweep time of 240 s. The modulation amplitude was set to 0.3 mT at a modulation frequency of 100 kHz. Microwave power was set to 0.63 mW. Time resolved measurements were done with a time delay of 60 s between experiments. The *in operando* experiment took 480 h, with 5983 individual EPR spectra recorded.

EPR data analysis

For the quantitative EPR analysis, spectra were baseline corrected and all three ruby signals were fitted with a phase adaptable Lorentzian line and afterwards subtracted. The outer two ruby signals were used for phase and amplitude correction. Due to the large width of the LNMO EPR resonance, a quantification of the signal amplitude by double integration is not reliable and would merely allow for a qualitative data assesment.[31] Due to the varying contributions from Mn and Ni at different oxidation states to the EPR signal, a quantitative fitting of the data using analytical expressions for exchange narrowed resonances would require not only extensive calibration measurements but also additional theoretical work to be conducted, which was outside the scope of this study. We resorted to a semi-quantitative fitting of the LNMO signal with Lorentzian lines, which was described in more detail in Ref. 31. The analysis of the EPR spectrum was performed with the phase obtained by the ruby reference and, finally, the obtained LNMO intensity was normalized using the ruby amplitude.

[1] A. Manthiram, K. Chemelewski, and E.-S. Lee, Energy Environ. Sci. **7**, 1339 (2014).

[2] R. Santhanam and B. Rambabu, J. Power Sources **195**, 5442 (2010).

[3] A. Brandt, A. Balducci, U. Rodehorst, S. Menne, M. Winter, and A. Bhaskar, J. Electrochem. Soc. **161**, A1139 (2014).

[4] N. Kiziltas-Yavuz, A. Bhaskar, D. Dixon, M. Yavuz, K. Nikolowski, L. Lu, R.-A. Eichel, and H. Ehrenberg, J. Power Sources **267**, 533 (2014).

[5] J. Cabana, M. Casas-Cabanas, F. O. Omenya, N. A. Chernova, D. Zeng, M. S. Whittingham, and C. P. Grey, Chem. Mater. **24**, 2952 (2012).

[6] M. Börner, P. Niehoff, B. Vortmann, S. Nowak, M. Winter, and F. M. Schappacher, Energy Technol. **4**, 1631 (2016).

[7] K. Shimoda, M. Murakami, H. Komatsu, H. Arai, Y. Uchimoto, and Z. Ogumi, J. Phys. Chem. C **119**, 13472 (2015).

[8] J. Rana, S. Glatthaar, H. Gesswein, N. Sharma, J. R. Binder, R. Chernikov, G. Schumacher, and J. Banhart, J. Power Sources **255**, 439 (2014).

[9] S. Bauer, L. de Biasi, S. Glatthaar, L. Toukam, H. Gesswein, and T. Baumbach, Phys. Chem. Chem. Phys. **17**, 16388 (2015).

[10] L. Boulet-Roblin, P. Borel, D. Sheptyakov, C. Tessier, P. Novák, and C. Villevieille, J. Phys. Chem. C **120**, 17268 (2016).

[11] G. Klinser, S. Topolovec, H. Kren, S. Koller, W. Goessler, H. Krenn, and R. Würschum, Appl. Phys. Lett. **109**, 213901 (2016).

[12] S. Topolovec, H. Kren, G. Klinser, S. Koller, H. Krenn, and R. Würschum, J. Solid State Electrochem. **20**, 1491 (2016).

[13] Z. Moorhead-Rosenberg, D. W. Shin, K. R. Chemelewski, J. B. Goodenough, and A. Manthiram, Appl. Phys. Lett. **100**, 213909 (2012).

[14] N. Amdouni, K. Zaghib, F. Gendron, A. Mauger, and C. M. Julien, J. Magn. Magn. Mater. **309**, 100 (2007).

[15] A. Bhaskar, N. N. Bramnik, A. Senyshyn, H. Fuess, and H. Ehrenberg, J. Electrochem. Soc. **157**, A689 (2010).

[16] J.-H. Kim, S.-T. Myung, C. S. Yoon, S. G. Kang, and Y.-K. Sun, Chem. Mater. **16**, 906 (2004).

[17] L. Wang, H. Li, X. Huang, and E. Baudrin, Solid State Ionics **193**, 32 (2011).

[18] H. Xia, Y. S. Meng, L. Lu, and G. Ceder, J. Electrochem. Soc. **154**, A737 (2007).

[19] H. Duncan, B. Hai, M. Leskes, C. P. Grey, and G. Chen, Chem. Mater. **26**, 5374 (2014).

[20] E. Lee and K. A. Persson, Energy Environ. Sci. **5**, 6047 (2012).

[21] K. Dokko, M. Mohamedi, N. Anzue, T. Itoh, and I. Uchida, J. Mater. Chem. **12**, 3688 (2002).

[22] M. Kunduraci, J. F. Al-Sharab, and G. G. Amatucci, Chem. Mater. **18**, 3585 (2006).

[23] H. Shiiba, N. Zettsu, M. Nakayama, S. Oishi, and K. Teshima, J. Phys. Chem. C **119**, 9117 (2015).

[24] C. Masquelier, M. Tabuchi, K. Ado, R. Kanno, Y. Kobayashi, Y. Maki, O. Nakamura, and J. B. Goodenough, J. Solid State Chem. **123**, 255 (1996).

[25] A. Abragam and B. Bleaney, *Electron Paramagnetic Resonance of Transition Ions* (Oxford University Press, 2012).

[26] J. B. Goodenough, *Magnetism and the Chemical Bond* (Interscience Publishers, New York, London, Sydney, 1963).

[27] P. W. Anderson and P. R. Weiss, Rev. Mod. Phys. **25**, 269 (1953).

[28] A. Niemöller, P. Jakes, S. Kayser, Y. Lin, W. Lehnert, and J. Granwehr, J. Magn. Reson. **269**, 157 (2016).

[29] P. P. R. M. L. Harks, F. M. Mulder, and P. H. L. Notten, J. Power Sources **288**, 92 (2015).

[30] C. P. Grey and J. M. Tarascon, Nat. Mater. **16**, 45 (2016).

[31] J. Wandt, C. Marino, H. A. Gasteiger, P. Jakes, R.-A. Eichel, and J. Granwehr, Energy Environ. Sci. **8**, 1358 (2015).

[32] J. Wandt, P. Jakes, J. Granwehr, H. A. Gasteiger, and R.-A. Eichel, Angew. Chem., Int. Ed. **55**, 7006 (2016).

[33] M. Sathiya, J.-B. Leriche, E. Salager, D. Gourier, J.-M. Tarascon, and H. Vezin, Nat. Commun. **6**, 6276 (2015).

[34] I. A. Shkrob, A. J. Kropf, T. W. Marin, Y. Li, O. G. Poluektov, J. Niklas, and D. P. Abraham, J. Phys. Chem. C **118**, 24335 (2014).

[35] G. Blasse, J. Phys. Chem. Solids **27**, 383 (1966).

[36] T. Nakamura, Y. Yamada, and M. Tabuchi, J. Appl. Phys. **98**, 093905 (2005).

[37] Z. Moorhead-Rosenberg, K. R. Chemelewski, J. B. Goodenough, and A. Manthiram, J. Mater. Chem. A **1**, 10745 (2013).